

**Magnetic & Chemical Non-Uniformity in $\text{Ga}_{1-x}\text{Mn}_x\text{As}$
as Probed with Neutron & X-Ray Reflectometry**

B. J. Kirby

Department of Physics and Astronomy, University of Missouri, Columbia, Missouri 65211, USA and
Manuel Lujan Jr. Neutron Scattering Center, Los Alamos National Laboratory, Los Alamos, New Mexico 87545, USA

J. A. Borchers

NIST Center for Neutron Research, National Institute of Standards and Technology, Gaithersburg, Maryland 20899, USA

J. J. Rhyne

Manuel Lujan Jr. Neutron Scattering Center, Los Alamos National Laboratory, Los Alamos, New Mexico 87545, USA

K. V. O'Donovan

NIST Center for Neutron Research, National Institute of Standards and Technology, Gaithersburg, Maryland 20899, USA and
Department of Physiology and Biophysics, University of California, Irvine, California 92697

S. G. E. te Velthuis

Materials Science Division, Argonne National Laboratory, Argonne, Illinois 60439, USA

S. Roy

Advanced Light Source, Lawrence Berkeley National Laboratory, Berkeley, California 94720, USA

Cecilia Sanchez-Hanke

National Synchrotron Light Source, Brookhaven National Laboratory, Upton, New York 11973, USA

T. Wojtowicz

Department of Physics, University of Notre Dame, Notre Dame, Indiana 46556, USA and
Institute of Physics of the Polish Academy of Sciences, 02-688 Warsaw, Poland

X. Liu, W. L. Lim, M. Dobrowolska and J. K. Furdyna

Department of Physics, University of Notre Dame, Notre Dame, Indiana 46556, USA

Abstract

We report on annealing dependent phenomena in $\text{Ga}_{1-x}\text{Mn}_x\text{As}$ films, as examined using polarized neutron and x-ray reflectometry. Measurements were performed on three sets of as-grown and optimally annealed $\text{Ga}_{1-x}\text{Mn}_x\text{As}$ thin film pairs. For two of the sets, annealing is observed to smooth pronounced magnetization gradients, and alter the films' surface chemical composition. The third set is different, as it is found to have a higher as-grown Curie temperature, features no detectable magnetization gradient (as-grown or annealed), and annealing does not alter the surface chemical composition as drastically as for the other two sets. Our results demonstrate the effects of annealing on the $\text{Ga}_{1-x}\text{Mn}_x\text{As}$ depth profile, and suggest that the depth profile is very sensitive to growth conditions. Furthermore, this work illustrates how polarized neutron reflectometry can be used to measure the magnetic depth profiles of extremely dilute magnetic thin films ($M < 50 \text{ emu}\cdot\text{cm}^{-3}$).

PACS numbers: 75.50.Pp, 61.12.Ha, 75.70.Ak, 71.55.Eq

I. Introduction

In recent years, there has been widespread interest in the development of spintronics technology – electronic devices that exploit the spin degree of freedom of charged particles. Particular attention has been focused on fabrication of ferromagnetic dilute magnetic semiconductors (DMS), due to their potential as effective spin injectors in spintronic devices [1,2,3]. The ferro-DMS system at the forefront of this research effort has been $\text{Ga}_{1-x}\text{Mn}_x\text{As}$ [4,5]. The ferromagnetic behavior in $\text{Ga}_{1-x}\text{Mn}_x\text{As}$ originates from coupling between spin 5/2 Mn^{2+} ions that occupy Ga sites in the lattice (Mn_{Ga}) [6]. The coupling is thought to be similar to the RKKY interaction in metals, where the ferromagnetic exchange is mediated by charge carriers [7]. For $\text{Ga}_{1-x}\text{Mn}_x\text{As}$ it is widely accepted that Mn_{Ga} are acceptors, and that they communicate their spin orientation among each other via self-generated holes [8].

While $\text{Ga}_{1-x}\text{Mn}_x\text{As}$ thin films can be produced with ferromagnetic transition temperatures impressive for a true DMS ($T_C > 150$ K [9,10,11]), the ferromagnetic quality of a given $\text{Ga}_{1-x}\text{Mn}_x\text{As}$ sample is highly sensitive to growth conditions, and post-growth treatment. In particular, it has been shown that post-growth annealing of $\text{Ga}_{1-x}\text{Mn}_x\text{As}$ at temperatures near or below the growth temperature greatly enhances T_C [12], and can increase the saturation magnetization M [13]. Additionally, the T_C enhancement effect is strongly dependent on the annealing temperature, and on the annealing time [9,13]. To understand the annealing process, one must consider an unwanted impurity, Mn at interstitial sites (Mn_{I}) [14,15,16]. Mn_{I} act as double donors – neutralizing holes needed to mediate the ferromagnetic exchange. Furthermore, calculations suggest that when in close proximity, Mn_{I} and Mn_{Ga} exhibit an *antiferromagnetic* exchange interaction, resulting in an overall reduction in M [16]. Formation of Mn_{I} in $\text{Ga}_{1-x}\text{Mn}_x\text{As}$ is likely determined by the thermodynamics of the growth process [17], explaining why precise control of growth

conditions is necessary for samples of high ferromagnetic quality.

Evidence now exists to suggest that annealing of $\text{Ga}_{1-x}\text{Mn}_x\text{As}$ thin films reduces the amount of Mn_{I} in the film and increases the amount of Mn at the film surface. Such evidence includes experiments utilizing Rutherford backscattering and particle induced x-ray emission [17], Auger spectroscopy and transport measurements [9], and polarized neutron reflectivity (PNR) [18,19]. Additionally, annealing studies of $\text{Ga}_{1-x}\text{Mn}_x\text{As}$ films capped with GaAs show that the GaAs cap ruins the annealing process – further suggesting that annealing works by diffusing impurities to the surface [19,20,21].

Reflectometry is a powerful experimental technique that is sensitive to buried interfaces of thin films. PNR is sensitive to depth-dependent magnetic and chemical composition [22,23,24,25,26], while x-ray reflectometry (XRR) used in the way we describe, is sensitive to the depth-dependent charge density [27,28]. Therefore, these techniques are quite powerful in tandem, as they provide complementary information. Reflectivity's depth sensitivity makes it a natural tool with which to examine the effects of annealing on $\text{Ga}_{1-x}\text{Mn}_x\text{As}$, since vertical impurity diffusion is believed to play such a critical role in enhancing the ferromagnetic exchange. However, PNR measurements of $\text{Ga}_{1-x}\text{Mn}_x\text{As}$ push the limits of the technique, due to the minute magnetization ($M \approx 10\text{-}50 \text{ emu}\cdot\text{cm}^{-3}$) of this material.

In this paper, we present reflectivity results for a series of $\text{Ga}_{1-x}\text{Mn}_x\text{As}$ films that were grown and annealed one after the other under very similar conditions. These results show the effects of annealing on the films' depth-profiles, suggest an extreme sensitivity of the depth profiles to growth conditions, and demonstrate approaches for understanding the subtle magnetic signals encoded in the neutron reflectivity of such a dilute ferromagnet.

II. Reflectivity

Our PNR measurements were taken using the NG-1 Reflectometer at the NIST Center for Neutron Research (NCNR), while rotating anode XRR measurements were conducted with the x-ray diffraction facilities at the Lujan Neutron Scattering Center.

For the PNR measurements, the sample was mounted in a closed-cycle cryostat, and a magnetic field H was applied in the plane of the film. Using Fe/Si supermirrors in conjunction with Al-coil flippers, incident neutrons of wavelength $\lambda = 4.75$ Å were polarized to have their spin either parallel or anti-parallel to H , and were reflected from the film surface. Upon specular reflection, another flipper/supermirror pair and a ^3He pencil detector were used to measure the two non spin-flip (NSF) reflectivities R_{++} and R_{--} , and the two spin-flip (SF) reflectivities R_{+-} and R_{-+} , each as a function of wavevector transfer Q . Background was measured by performing the above described measurements at 0.3° away from the specular condition, and was subtracted from the specular data. Additionally, the data were corrected for polarization efficiency, and non-uniform sample illumination (footprint correction).

The XRR measurements were conducted in a similar manner, but at room temperature, and in zero applied field. Cu K_α x-rays were reflected from the sample ($\lambda = 1.45051$ Å), and then detected using a 1-dimensional position sensitive detector (PSD). Use of the PSD allowed for simultaneous measurement of the specular reflectivity and the off-specular background scattering (which was subtracted from the specular).

A sample's reflectivity $R(Q)$ is a function of the Fourier transform of the sample's depth-dependent scattering length density (SLD) $\rho(z)$. For neutrons, the SLD has both chemical [29] and magnetic components

Total Neutron SLD:

$$\rho(z) = \rho_{\text{chem}}(z) + \rho_{\text{mag}}(z), \quad (1)$$

Chemical SLD:

$$\rho_{\text{chem}}(z) = \sum_i N_i(z) b_i, \quad (2)$$

Magnetic SLD:

$$\rho_{\text{mag}}(z) = C \sum_i N_i(z) \mu_i = C' M, \quad (3)$$

where the summation is over each type of atom in the system, b is the nuclear scattering length, μ is the magnetic moment in Bohr magnetons (μ_B), and M is the magnetization. The constants $C = 2.695 \cdot 10^{-5}$ Å· μ_B , and $C' = 2.9 \cdot 10^{-9}$ emu $^{-1} \cdot \text{cm}^3 \cdot \text{\AA}^{-2}$ [26]. N is the in-plane average of the number density, and is a function of x . We have calibrated x-ray diffraction (XRD) measurements of our samples with results with from particle induced x-ray emission (PIXE) measurements of similar samples we have grown, providing a reliable relation between the lattice parameter a and x [30,31],

$$a(x) = (5.65469 + 0.24661x) \text{\AA}. \quad (4)$$

From Eq. 4, the number density is calculated

$$N(x) = 4 [a(x)]^3. \quad (5)$$

The x-ray SLD is dependent on the charge density [27,28]

X-Ray SLD:

$$\rho_{x\text{-ray}}(z) = r_e \sum_i N_i(z) Z_i, \quad (6)$$

where Z is the atomic number, and $r_e = 2.81 \times 10^{-5}$ Å, the classical radius of the electron.

Therefore, information about depth-dependent sample properties can be obtained by fitting the reflectivities to SLD models. Via a charge-density model, XRR provides information about chemical composition, but not magnetic composition. For the case of polarized neutrons it can be shown [22-26] that:

- A) The two NSF reflectivities provide chemical *and* magnetic information, as they are sensitive to $\rho_{chem}(z)$, and $M(z)$ (primarily the component of M parallel to H).
- B) The two SF reflectivities are totally magnetic in origin, and are sensitive to the component of $M(z)$ perpendicular to H .

For $\text{Ga}_{1-x}\text{Mn}_x\text{As}$ on a GaAs substrate, XRR and PNR are particularly complementary, as the two methods are sensitive to different aspects of that system's chemical composition. There is only an 11 % difference in Z for Ga and Mn. So, for $x \approx 0.05 - 0.10$, the difference in ρ_{x-ray} for GaAs and $\text{Ga}_{1-x}\text{Mn}_x\text{As}$ is small enough that x-rays are virtually insensitive to the interface between them. Therefore, the XRR measurements discussed in this paper provide information only about foreign material residing on the $\text{Ga}_{1-x}\text{Mn}_x\text{As}$ free surface. The case is quite different for PNR, as there is a 310 % difference in b for Ga and Mn [32]. Thus, even for small values of x , ρ_{chem} is measurably different for $\text{Ga}_{1-x}\text{Mn}_x\text{As}$ and GaAs – making the $\text{Ga}_{1-x}\text{Mn}_x\text{As}/\text{GaAs}$ interface, and the chemical properties of the $\text{Ga}_{1-x}\text{Mn}_x\text{As}$ layer detectable with PNR. Using equations 2 and 6, Figure 1 illustrates the difference in contrast for neutrons and x-rays by plotting the $\text{Ga}_{1-x}\text{Mn}_x\text{As}$ SLD divided by the SLD for undoped GaAs as a function of x [33].

Quantitative information about a sample is commonly obtained by employing a nonlinear least-squares numerical analysis to find a SLD model that produces a fit to the data with the lowest possible value of χ^2 [34]. The PNR data described in this paper were fit in this way using the Reflpol software package [35,36], while the XRR data was fit using the co_refine fitting program [25]. Both of these programs are based upon the dynamical formalism of Parratt [37]. The SLD models used to fit the neutron data in this paper required division of the $\text{Ga}_{1-x}\text{Mn}_x\text{As}$ layer into multiple sublayers, because an inhomogeneous magnetization as a function of depth was required to properly fit the reflectivities for several of the samples. For these models, the chemical SLD was

also allowed to vary among sublayers, to account for the possibility of large-scale Mn diffusion. A variety of models were explored in order to ensure that the magnetic and chemical features in the SLD models were not *interdependent* in the fit.

III. Sample Preparation

Using molecular-beam epitaxy, three separate $\text{Ga}_{1-x}\text{Mn}_x\text{As}$ samples were fabricated one after the other via the following steps:

- 1) 300 nm GaAs buffer layer was deposited at ~ 580 °C on a [001] GaAs substrate, held in place by Indium on a Mo block.
- 2) The substrate was cooled to ~ 210 °C, and a 3 nm GaAs buffer layer was deposited.
- 3) While still at ~ 210 °C, a $\text{Ga}_{1-x}\text{Mn}_x\text{As}$ layer of variable thickness was grown.
- 4) Following growth, each sample was cleaved into pieces - one piece for annealing, and one piece to be left as-grown.
- 5) Annealing took place at ~ 270 °C, for about 1 hour, in a N_2 environment.
- 6) The samples were further divided, providing specimens for bulk characterization, and pieces for PNR measurements.

While each of the sample sets were grown at *nominally* the same temperature (the sample holders were measured to be at the same temperature), small variations in heat capacity for the individual Mo sample holders likely resulted in slightly different temperatures at the substrate surface during growth. This point is important, as it may partially account for differences among the sample sets.

The result was three sets of as-grown/annealed pairs (labeled Sets A, B, and C), with $\text{Ga}_{1-x}\text{Mn}_x\text{As}$ thicknesses of 50 nm, 100 nm, and 50 nm, respectively. The Mn_{Ga} concentration x , in the $\text{Ga}_{1-x}\text{Mn}_x\text{As}$ samples was established from XRD measurements of the as-grown pieces using Eq. 4. The uncertainty associated with determination of x in this way is $\sim \pm 0.01$. Primary characterization of the samples was done by using Hall Effect to

measure the apparent hole concentration p [38], and transport measurements to measure the resistivity \tilde{n} , and T_C . These properties are summarized in Table 1. Based upon extensive results from similar samples [39,40], the magnetic easy axis of these samples was believed to lie along [100] at temperatures < 20 K.

IV. Experimental Results & Discussion

Reflectometry was used to examine the three sets of $\text{Ga}_{1-x}\text{Mn}_x\text{As}$ as-grown/annealed pairs, each of which demonstrated significant increases in T_C upon annealing. The aim of these experiments was to search for depth-dependent changes that occur during annealing, with the hope of better understanding the mechanisms that enhance the ferromagnetic exchange. Annealing was found to significantly alter the chemical and magnetic depth profiles of Sets A and B, while it had little effect on the depth profiles of Set C.

The first as-grown/annealed $\text{Ga}_{1-x}\text{Mn}_x\text{As}$ pair considered provides the clearest evidence of an annealing-dependent depth profile, and is denoted as Set A. Set A has approximately 500 Å $\text{Ga}_{1-x}\text{Mn}_x\text{As}$ film thickness, and the Mn_{Ga} concentration was determined to be $x \approx 0.092$. For the as-grown sample, magnetotransport measurements revealed a maximum resistivity of $\tilde{n} \approx 0.035 \Omega\cdot\text{cm}$, at $T_C \approx 55$ K. For the annealed sample, $\tilde{n} \approx 0.005 \Omega\cdot\text{cm}$ at $T_C \approx 125$ K. The increased T_C shows that annealing certainly improved the ferromagnetic exchange. Additionally, the drop in resistivity is consistent with an increased carrier concentration. Since Mn_{I} are donors, Mn_{Ga} are acceptors, and the ferromagnetic exchange is mediated via holes, an increased carrier concentration coupled with an increased T_C is consistent with a reduction in Mn_{I} after annealing.

A set of PNR measurements was taken on each of the samples after cooling them to low temperature ($T = 16$ K for the as-grown, $T = 18$ K for the annealed) while in an in-plane field of $H = 6.6$ kOe. The samples were oriented with a [100] axis

oriented nominally parallel to H . Both non spin-flip (NSF) and spin-flip (SF) data were taken. However, the SF data were found to be negligible, and were not measured with the same statistics as the NSF.

Figure 2 compares the individual NSF reflectivities and fits corresponding to the as-grown and annealed samples. The spin-down (R_{-}) reflectivities are shown at the top, and the spin-up (R_{++}) are shown at the bottom. For large Q Porod's Law requires $R \propto Q^4$ [25], so the data and fits are multiplied by Q^4 in order to simultaneously visualize features at low and high- Q regions. It can be seen that the fits are good, but in order to extract meaningful information about the sample it is critical to *qualitatively* examine the features that differ for the two samples, and to understand how those features correlate to characteristics of the models that result from the fitting.

In Figure 2, the frequency of the annealed sample's oscillations is larger than that of the as-grown. Since oscillation frequency is determined by layer thicknesses in the sample, this difference shows that the annealed sample is thicker than the as-grown. Furthermore, at low- Q the as-grown and annealed sample have reflectivities of similar intensity, while at high- Q the annealed sample's reflectivity is consistently more intense than that of the as-grown. Fitting reveals that this difference is due to an increased surface chemical SLD for the annealed sample as compared to the as-grown.

More can be assessed by looking at the as-grown and annealed samples' data separately, and considering the difference between the spin-up and spin-down reflectivities. Since the difference between the two spin states originates from the sample magnetization, such analysis can shed light on the magnetic properties of the samples. Due to this system's low magnetization these differences are subtle, but they become readily apparent by recasting the spin-up and spin-down reflectivities and fits in terms of spin asymmetry (SA),

$$SA = (R_{++} - R_{-}) / (R_{++} + R_{-}). \quad (6)$$

Figure 3 shows each sample's reflectivities and fits manifested as spin asymmetry [41]. The amplitudes of the low- Q spin asymmetry peaks are clearly larger for the annealed sample. This difference is due to a larger net magnetization for the annealed sample as compared to the as-grown. The Q -definition of the spin asymmetry peaks is also quite different for the two samples. Especially at low- Q , the as-grown sample's peaks are less clearly resolved (smeared), while the annealed sample's peaks are much more sharply defined. The fitting is highly sensitive to this smearing, and shows it to be due to a pronounced gradient in the magnetization. At higher- Q , the spin asymmetry for the annealed sample frequently crosses zero, while that of the as-grown sample only shows a single crossing at the highest- Q . Fitting shows that this zero crossing results from a drop in magnetization at the sample surface. That this feature is more pronounced for the annealed sample is due to a more drastic drop in surface magnetization as compared to the as-grown.

The SLD models that produce the best fit to the neutron data are shown in Figure 4. The chemical SLD corresponds to a dashed line at the top of each panel, while the magnetic SLD is the solid line at the bottom of each panel. The sample magnetization is directly proportional to the magnetic SLD (see Equation 3), and is plotted relative to a separate scale on the right-hand axis. Note the breaks in the vertical axes, and the difference in scale for the annealed and as-grown magnetic SLD's. The $\text{Ga}_{1-x}\text{Mn}_x\text{As}$ sample is clearly delineated from the GaAs substrate in each model, and corresponds to a region of decreased chemical SLD, and non-zero magnetic SLD.

The model for the as-grown sample shows that throughout the bulk of the sample, the chemical SLD is flat, while the magnetization features a pronounced spatial gradient. The magnetization doubles from one side to the other while the chemical SLD does not show a comparable change, implying that the magnetization gradient is *not* due to changes in total Mn concentration. A more likely explanation is that the *ratio* of Mn_{Ga} to Mn_{I}

changes from substrate to surface, while the *overall* Mn concentration remains relatively constant. The model's *integrated* magnetization (the value that would be obtained through bulk magnetometry) is calculated by integrating over the magnetization of the entire sample, and dividing by the sample thickness. The integrated magnetization for the model of the as-grown sample in Fig. 4 is $22 \text{ emu}\cdot\text{cm}^{-3}$.

Since the presence of a magnetization gradient is determined from very subtle features in the data, it is worthwhile to compare the as-grown fit from Fig. 3 to a fit originating from a flat magnetization model. The top panel of Figure 5 shows the graded as-grown model from Fig 4 plotted with a flat magnetization model. The bottom panel shows the fits corresponding to those respective models, plotted with the as-grown data (cast as spin asymmetry). The flat model (which does allow for reduced magnetization near the surface) fails spectacularly in describing the low- Q spin asymmetry, as it neither accounts for the broadness of the peaks, nor reproduces the smearing of the peaks – resulting in a χ^2 over five times larger than that of the best-fit gradient model [42]. Figure 4 shows the magnetization gradient to extend for about 450 \AA , and while this model does provide the *best* fit to the data, models with gradients of as little as 170 \AA produce fits of only slightly reduced quality. Despite this spatial uncertainty, each of the competing models agree in that they feature low magnetization at the substrate, a magnetization gradient with an approximate factor of two increase that peaks just below the surface, and reduced magnetization at the surface.

The model for the annealed sample (Fig. 4) features some drastic differences [43]. First, it reveals a large increase in saturation magnetization, as the model's integrated magnetization is $48 \text{ emu}\cdot\text{cm}^{-3}$. For the majority of the $\text{Ga}_{1-x}\text{Mn}_x\text{As}$ film thickness, chemical SLD and the magnetization are both constant. This result suggests that the overall Mn concentration is again constant throughout the annealed $\text{Ga}_{1-x}\text{Mn}_x\text{As}$ film, but the ratio of Mn_{Ga} to Mn_{I} is much more uniform than it is for the as-

grown. These annealing-dependent changes are highly consistent with a migration of Mn_I. However, if this is the case, a small increase in the chemical SLD of the annealed film near the substrate might be expected, corresponding to the fact that more Mn_I would have evacuated the region of depleted magnetization than any other. This can be reconciled, as Mn_I constitute only a small fraction of the total Mn [17]. Although the difference between GaAs and GaAs doped with ~9% Mn is readily apparent in Fig.4, a change in chemical SLD *within* the Ga_{1-x}Mn_xAs film resulting from Mn concentration changes of a few percent is probably too small to be detected with PNR.

More evidence for redistribution of Mn_I during annealing can be found by comparing the surfaces of the as-grown and annealed films. For the as-grown film there is a small drop in surface magnetization, but very little change in surface chemical SLD. However, for the surface of the annealed film, the model shows a sharp increase in the chemical SLD, while the magnetization drastically drops toward zero – indicating a non-magnetic surface layer comprised of something other than Ga_{1-x}Mn_xAs. The neutron data show this surface layer to be about 50 Å thick, and it accounts for the difference in oscillation frequency between the as-grown and annealed samples (Fig. 2).

To further explore the differences between as-grown and annealed, consider Figure 6, which shows the XRR data and fits for the two samples, with the resulting SLD models shown in the inset. The x-axis of the annealed sample's SLD model has been shifted so that for both models the region where the SLD begins to drop off is shown at approximately the same depth. Additionally, the annealed sample's SLD has been normalized such that the small difference in Ga_{1-x}Mn_xAs SLD between as-grown and annealed is eliminated [43]. Figure 6 shows the reflectivities to be very different, and since XRR is insensitive to the Ga_{1-x}Mn_xAs/GaAs interface, this further suggests that annealing significantly altered the *surface* of the Ga_{1-x}Mn_xAs film. Both samples show two

oscillations between $Q = 0.1 \text{ \AA}^{-1}$ and $Q = 0.4 \text{ \AA}^{-1}$, but for the as-grown sample these oscillations are unresolved and are almost indistinguishable from one another, while for the annealed sample, the oscillations are very well-defined. The fact that oscillations are present at all for the as-grown sample shows that there is foreign material present on the surface of the Ga_{1-x}Mn_xAs film even before annealing.

The SLD models reveal that annealing sharpens the rough “mound” of increased SLD observed near 50 Å in the as-grown model, and makes the SLD falloff to zero much rougher. This suggests that annealing “cleaned up” the top Ga_{1-x}Mn_xAs interface, and added approximately 20 Å of foreign surface material. This is in good qualitative agreement with the PNR results for these samples. The fact that PNR and XRR do not agree *quantitatively* about the thickness of material added by annealing is not surprising, given that the surface layer is a rough aggregation of material, resulting in an interface that is not sharply defined.

In addition, we also examined the Set A samples using *resonant* XRR at Beamline X13A of Brookhaven National Laboratory's National Synchrotron Light Source. In this measurement, the intensity of x-rays reflected from the sample was recorded as a function of incident x-ray energy, at a fixed reflection angle. In this way the presence of a particular element can be detected via peaks or dips in the reflected intensity corresponding to electronic transitions for that element [44]. This sensitivity allowed us to probe differences in chemical composition between the as-grown and annealed sample. Figure 7 shows the reflected x-ray intensity as function of energy for the as-grown and annealed samples. Both the as-grown and annealed films have similar sharp features around 450 eV. We are not completely certain of the origin of these features, but we speculate they could be due to indium, since they occur near the indium M₄3d_{3/2} electron binding energy (451.4 eV). If so, it would suggest that a small amount of In (which was used in the MBE chamber) is present in both the as-grown and annealed samples in similar

quantities [45]. However, it is the *annealing-dependent* features that are most interesting. The annealed sample displays much more distinct features near the oxygen K1s (543.1 eV), manganese L₃2p_{3/2} (638.7 eV), and the manganese L₂2p_{1/2} (649.9 eV) electron binding energies than does the as-grown sample. Since this type of measurement is most sensitive to composition near the film surface, these results suggest that annealing increases the concentration of Mn and O at the film surface.

The combination of the PNR and XRR data suggest that while there is some foreign material present on the surface of the as-grown film (possibly some sort of native oxide or nitride layer), there is extra foreign material (likely MnO and/or MnN) present after annealing. We have been unable to find a compound that can simultaneously explain the observed chemical SLD and x-ray SLD at the surface of these films [46]. This, coupled with the jaggedness of the SLD profiles needed to fit the x-ray data suggest that these surfaces are quite rough, disordered, and could be comprised of several different compounds.

We next discuss Set B, for which some PNR results have already been described in Ref. 18. This as-grown/annealed pair is approximately 1000 Å thick, and the Mn_{Ga} concentration is $x \approx 0.076$. For the as-grown sample, magnetotransport measurements revealed a maximum resistivity of $\tilde{n} \approx 0.036 \Omega \cdot \text{cm}$ at $T_C \approx 60 \text{ K}$. For the annealed sample, $\tilde{n} \approx 0.006 \Omega \cdot \text{cm}$ at $T_C \approx 125 \text{ K}$. These resistivities and T_C 's are similar to those of Set A, and again suggest a decrease in Mn_I concentration with annealing. Superconducting quantum interference device (SQUID) magnetometry results revealed annealing increased the saturation magnetization (from 20 to 40 emu cm⁻³), and confirm the increase in T_C .

PNR measurements were taken after zero-field cooling the samples to $T = 13 \text{ K}$, and applying $H = 1 \text{ kOe}$ in-plane. The samples were oriented with a [110] direction nominally parallel to H [47]. SF data was taken with equal statistics to the NSF data, and was found to be minimal. We note that the

quality of these data are somewhat reduced compared to those for Set A due to differences in counting time and point density.

Figure 8 compares the NSF spin-up and spin-down reflectivities and fits for the as-grown and annealed samples. While annealing-dependent differences in frequency are more difficult to discern than for Set A, Figure 8 shows increased high- Q intensity for the annealed sample – the result of an increased surface chemical SLD. The important magnetic features for Set B are also very similar to that of Set A, and are accentuated in the spin asymmetries for the two samples, shown in Figure 9. It can be seen that annealing increases the peak amplitude, and decreases the smearing of the peaks somewhat (especially in proportion to the *amplitude* of the peaks) – due to an increased and more homogeneous magnetization upon annealing. Both samples show a decrease in peak amplitude at high- Q (due to reduced magnetization at the surface), but the annealed sample spin-asymmetry prominently crosses zero (due to a more drastic drop in magnetization).

The best fits for this data were generated with the SLD models shown in Figure 10. These models corroborate the SQUID measurements fairly well, as they show that annealing increases the integrated magnetization from 17 emu·cm⁻³ to 48 emu·cm⁻³. The models are qualitatively very similar to those for Set A. Again we see a pronounced magnetization gradient for the as-grown sample, and very little change in the chemical SLD at the surface. For the annealed sample, the magnetization gradient is less extensive, and the top 50 Å of the annealed sample features a sharp increase in chemical SLD, and a sharp decrease in magnetization.

However, there is more uncertainty in the models of Set B as compared to those of Set A, due to increased sample thickness (which compresses the oscillations) and reduced data quality. This uncertainty is more pronounced for the as-grown sample. While the fitting is highly sensitive to the presence of a magnetization gradient, it is not very

sensitive to the spatial extent of the gradient. To illustrate the approximate range of possible spatial extents, Figure 11 shows a comparison of the “best-fit” 6-sublayer model from Figure 10 and a simpler 4-sublayer model. The two models have significant differences, as the 4-sublayer model has a larger integrated magnetization, and a less extensive magnetization gradient (about 400 Å for the 4-sublayer, 800 Å for the 6-layer). While the 4-sublayer fit cannot be ruled out, further reducing the spatial extent of the magnetization gradient progressively worsens the quality of the fit.

XRR results for Set B are shown in Figure 12. The Set B data were fit in a manner similar to that of Set A, and as was the case for Set A, the as-grown sample features two very smeared oscillations between $Q = 0.1 \text{ \AA}^{-1}$ and $Q = 0.4 \text{ \AA}^{-1}$, while the annealed sample shows two better defined oscillations in the same region of Q . The SLD models have been normalized and shifted in the same way as described for Set A. Annealing is shown to eliminate the mound of increased SLD seen at around 50 Å in the as-grown sample’s model, and adds a low SLD layer to the sample surface. This suggests that annealing cleaned up the top $\text{Ga}_{1-x}\text{Mn}_x\text{As}$ interface, and added foreign surface material, similar to Set A.

While Sets A and B are very similar, Set C is different. Set C is an as-grown/annealed pair of approximately 500 Å $\text{Ga}_{1-x}\text{Mn}_x\text{As}$ film thickness, with a Mn_{Ga} concentration of $x \approx 0.081$. Even though this sample was grown and annealed under nominally the same conditions as the previously discussed samples, magnetotransport measurements revealed some differences. The as-grown sample showed a maximum resistivity of $\tilde{n} \approx 0.009 \Omega\text{-cm}$ at $T_C \approx 70 \text{ K}$. This is a substantial increase in as-grown T_C as compared to the other two as-grown samples discussed (Table 1), suggesting an increase in hole concentration and a reduced Mn_{I} concentration. The as-grown \tilde{n} is noticeably lower for Set C, as compared to the other two, also consistent with increased hole concentration. For the annealed sample, $\tilde{n} \approx 0.003$

$\Omega\text{-cm}$ at $T_C \approx 140 \text{ K}$. This T_C is higher and \tilde{n} is lower than the other two annealed samples, again suggesting an increased hole concentration. These results are consistent with room-temperature Hall effect measurements, which show the Set C samples to have larger carrier concentrations, p than the other two sets (see Table 1). What all of this suggests is that the as-grown sample of Set C was somehow grown with a lower Mn_{I} concentration than those of Sets A and B, despite all of them being grown one after the other under very similar conditions!

PNR measurements were taken after applying $H = 6.6 \text{ kOe}$ in-plane, and cooling the samples to low temperature ($T = 20$ for the as-grown, $T = 16 \text{ K}$ for the annealed). The samples were oriented with a [100] direction nominally parallel to H . The quality of the data for the as-grown sample is reduced because of its small sample size (1.0 x 1.5 cm instead of the 2 x 2 cm size of the other samples), and increased instrumental background in the “mid- Q ” region of the scan. The scans for the annealed sample were of very high quality. For both samples, SF data were taken with lower statistics than the NSF data, but were found to be minimal.

Figure 13 shows a comparison of the as-grown and annealed samples for the spin-up and spin-down reflectivities and fits. In contrast to Sets A and B, the high- Q intensity of reflectivity is fairly similar for the two samples. In particular, there is no high- Q increase in intensity *relative* to low- Q . This lack of increased intensity at high- Q shows that annealing has less effect on the chemical SLD at the surface for Set C than it did for Sets A and B.

The measured and calculated (from the fits to the reflectivity) spin asymmetries for the as-grown and annealed samples are shown in Figure 14. This figure illustrates the magnetic similarities in the samples, especially at very low- Q . The amplitudes of the first peaks are very similar for both samples, due to an increase in magnetization upon annealing that is not as large as for the other sets. More importantly, there is no discernable difference in

low- Q peak smearing between the samples. This is because *neither* sample has a magnetization gradient. While the error bars for the as-grown sample increase significantly after the first peak, it appears that the peak amplitude does become noticeably larger for the annealed sample after that point, due to some increase in net magnetization. Both samples' spin asymmetries cross zero in similar ways, due to dropoffs in magnetization at the surface.

The as-grown and annealed SLD models used to fit the PNR data are shown in Figure 15. The as-grown sample's model shows relatively constant chemical and magnetic SLD's. Notice the absence of a magnetization gradient. There is great certainty in this feature of the model, as it results from the lack of smearing between the first two spin asymmetry peaks - something that occurs at Q -values where the statistics are still very good. There is a small feature in the chemical SLD near the substrate, but this is likely due to the reduced quality of the data at high- Q and should be ignored. At the surface of the as-grown sample we see a drop in the magnetization, accompanied by a small drop in the chemical SLD. The surface drop in magnetization is fairly reliable, as it originates from the spin-asymmetry crossing zero at high- Q - a very prominent feature of the data. However, the fit is much less sensitive to the drop in chemical SLD at the surface. The integrated magnetization for the model is $23 \text{ emu}\cdot\text{cm}^{-3}$.

Like Sets A and B, the model for the annealed sample shows an increase in the net magnetization (integrated magnetization is $37 \text{ emu}\cdot\text{cm}^{-3}$), although this increase is not as great as for the other sets. The magnetically active region of the annealed sample *appears* to be thicker, but the sensitivity of the fits to the as-grown sample thickness is too low to say this definitively (again due to the reduced data quality at high- Q). Other than these features, the model for the annealed sample is very similar to that of the as-grown. There is a region of decreased magnetization near the surface, but there is no spike in the chemical

SLD, meaning there is no neutron evidence for any increased foreign surface layer upon annealing.

However, XRR *does* provide evidence for some surface change upon annealing. XRR results for Set C are shown in Figure 16, and are somewhat different than the other two sets. The as-grown sample's reflectivity again shows two smeared oscillations between $Q = 0.1 \text{ \AA}^{-1}$ and $Q = 0.4 \text{ \AA}^{-1}$, but unlike the other two sets, annealing does not result in two *distinct* oscillations in this same region (although annealing does change the reflectivity). The inset of Figure 16 shows the SLD models, normalized and shifted in the same way as Sets A and B. Annealing is shown to eliminate the mound of increased SLD seen at around 50 \AA in the as-grown sample's model, and makes the SLD falloff to zero slightly rougher. This suggests that annealing cleaned up the top $\text{Ga}_{1-x}\text{Mn}_x\text{As}$ interface, and added some foreign surface material (although not as much as for the other two sets). That PNR could detect no change in surface composition, and XRR detected only a small change, suggests that annealing had a less drastic effect on the surface of the Set C than it did for the other two sets.

V. Conclusions

It is well known that annealing at the optimal temperature and time improves the ferromagnetic properties of $\text{Ga}_{1-x}\text{Mn}_x\text{As}$ films. Edmonds *et al.* have produced a theory of annealing in $\text{Ga}_{1-x}\text{Mn}_x\text{As}$, which proposes that annealing removes Mn_I from their lattice sites, and allows those liberated Mn ions to pacify themselves by moving to the free surface. This reduction in Mn_I increases the number of Mn participating in the ferromagnetic exchange, increases the concentration of holes that mediate that exchange, and thereby increases T_C . Our results strongly corroborate this theory. For all three sets of samples we observe that annealing increases the samples' net properties, p , T_C , and M in ways consistent with Mn_I out-diffusion - but it is our *depth-dependent* observations that are most compelling.

For Sets A and B - which have very similar as-grown values of T_C and p - we observe pronounced magnetization gradients before annealing. As explained earlier, we see no evidence that this gradient is due to a gradient in *total* Mn concentration, suggesting that the region near the substrate has a higher ratio of Mn_I/Mn_{Ga} than does the rest of the film. To explain this, consider that the lattice location of Mn (Ga site or interstitial) is strongly dependent on the thermodynamics during growth [17]. Therefore, the presence of a magnetization gradient might indicate that the mobility of Mn atoms was changing during the growth – possibly as a result of strong non-equilibrium growth, or even from time-dependent variations in the substrate temperature.

After annealing, the magnetization gradient is smoothed out, and we observe an increase in non-magnetic foreign material at the film surface. Resonant XRR suggests that this added material is rich in Mn and O. This magnetization smoothing and altering of surface chemistry provides powerful evidence that annealing does indeed diffuse Mn_I to the film surface.

Set C, which has higher as-grown T_C and p than the other two sets, features depth-dependent properties very different from Sets A and B. The as-grown sample of Set C has no magnetization gradient, suggesting a more uniform distribution of Mn_I , due to a more stable growth. Additionally, annealing of this sample produced a less drastic change in the film surface. It is possible that these two results are related – that the uniformity of the magnetization profile affects the mechanism through which Mn_I diffuses to the surface, resulting in a different surface chemistry after annealing.

Since these three sets of films were all grown under such similar conditions, the most likely cause of the differences among them is the variation in *actual* growth temperature that comes from the samples being grown on different Mo blocks. These results clearly illustrate the extreme sensitivity of the structural and magnetic properties of $Ge_{1-x}Mn_xAs$ to its growth conditions.

Work at Missouri and Notre Dame was supported by National Science Foundation Grant DMR-0138195, and the Missouri University Research Reactor Graduate Fellowship. Work at Los Alamos, Argonne, and Brookhaven was supported by the Office of Basic Energy Science, U. S. Dept. of Energy. Special thanks go to Chuck Majkrzak and Paul Kienzle of NIST, and Axel Hoffman of Argonne National Laboratory for their assistance with this work.

[1] Y. Ohno, D. K. Young, B. Beschoten, F. Matsukura, H. Ohno, and D. D. Awschalom, *Nature* **402**, 790 (1999).

[2] P. Van Dorpe, Z. Liu, W. Van Roy, V. F. Motsnyi, M. Sawicki, G. Borghs, and J. De Boeck, *Appl. Phys. Lett.* **84**, 3495 (2004).

[3] T. Jungwirth, K. Y. Wang, J. Mašek, K. W. Edmonds, Jürgen König, Jairo Sinova, M. Polini, N. A. Goncharuk, A. H. MacDonald, M. Sawicki, R. P. Campion, L. X. Zhao, C. T. Foxon, and B. L. Gallagher, *Phys. Rev. B* **72**, 165204 (2005).

[4] H. Ohno, A. Shen, F. Matsukura, A. Oiwa, A. Endo, S. Katsumoto, and Y. Iye, *Appl. Phys. Lett.* **69**, 363 (1996).

[5] Sawicki, *Journal of Magnetism and Magnetic Materials*, in press
[doi:10.1016/j.jmmm.2005.10.020](https://doi.org/10.1016/j.jmmm.2005.10.020), (2005).

[6] T. Dietl, H. Ohno, F. Matsukura, J. Cibert, D. Ferrand, *Science* **287**, 1019 (2000)

[7] Richard Bouzerar, Georges Bouzerar, and Timothy Ziman, *Phys. Rev. B* **73**, 024411 (2006).

[8] B. Beschoten, P. A. Crowell, I. Malajovich, D. D. Awschalom, F. Matsukura, A. Shen, and H. Ohno, *Phys. Rev. Lett.* **83**, 3073 (1999).

[9] K. Wang, R. Campion, K. Edmonds, M. Sawicki, T. Dietl, C. Foxon, and B. Gallagher, *AIP Conf. Proc.* **722**, 333 (2005).

[10] K. W. Edmonds, P. Boguslawski, K. Y. Wang, R. P. Campion, S. N. Novikov, N. R. S. Farley, B. L. Gallagher, C. T. Foxon, M. Sawicki, T. Dietl, M. B. Nardelli, and J. Bernholc, *Phys. Rev. Lett.* **92**, 37201 (2004).

[11] K. C. Ku, S. J. Potashnik, R. F. Wang, S. H. Chun, P. Schiffer, N. Samarth, M. J. Seong, A. Mascarenhas, E. Johnston-Halperin, R. C. Myers, A. C. Gossard, and D. D. Awschalom, *Appl. Phys. Lett.* **82**, 2302 (2003).

[12] T. Hayashi, Y. Hashimoto, S. Katsumoto, and Y. Iye, *Appl. Phys. Lett.* **78**, 1691 (2001).

[13] S. J. Potashnik, K. C. Ku, S. H. Chun, J. J. Berry, N. Samarth, and P. Schiffer, *Appl. Phys. Lett.* **79**, 1495 (2001).

[14] T. Wojtowicz, W. L. Lim, X. Liu, Y. Sasaki, U. Bindley, M. Dobrowolska, J. K. Furdyna, K. M. Yu, and W. Walukiewicz, *J. Superconductivity* **16**, 41 (2003).

[15] Georges Bouzerar, Timothy Ziman, and Josef Kudrnovsky, *Phys. Rev. B* **72**, 125207 (2005).

[16] J. Blinowski and P. Kacman, *Phys. Rev. B* **67**, 121204(R) (2003).

[17] K. M. Yu, W. Walukiewicz, T. Wojtowicz, I. Kuryliszyn, X. Liu, Y. Sasaki, and J. K. Furdyna, *Phys. Rev. B* **65**, 201303(R) (2002).

[18] B. J. Kirby, J. A. Borchers, J. J. Rhyne, S. G. E. te Velthuis, A. Hoffmann, K. V. O'Donovan, T. Wojtowicz, X. Liu, W. L. Lim, and J. K. Furdyna, *Phys. Rev. B* **69**, 81307(R) (2004).

[19] B. J. Kirby, J. A. Borchers, J. J. Rhyne, K. V. O'Donovan, T. Wojtowicz, X. Liu, Z. Ge, S. Shen, and J. K. Furdyna, *Appl. Phys. Lett.* **86**, 072506 (2005).

[20] D. Chiba, K. Takamura, F. Matsukura, and H. Ohno, *Applied Physics Letters* **82**, 3020 (2003).

[21] M. B. Stone, K. C. Ku, S. J. Potashnik, B. L. Sheu, N. Samarth, and P. Schiffer, *Appl. Phys. Lett.* **83**, 4568 (2003).

[22] G. P. Felcher, *Phys. Rev. B* **24**, R1595 (1981).

[23] G. P. Felcher, R. O. Hileke, R. K. Crawford, J. Haumann, R. Kleb, and G. Ostrowski, *Rev. Sci. Inst.* **58**, 609 (1987).

[24] C. F. Majkrzak, *Physica B* **173**, 75 (1991).

[25] J. F. Ankner and G. P. Felcher, *Journal of Magnetism and Magnetic Materials* **200**, 741 (1999).

[26] C. F. Majkrzak and M. R. Fitzsimmons, *Modern Techniques for Characterizing Magnetic Materials*, edited by Zimei Zhu (Kluwer, Boston 2005), pp. 107-155.

[27] T. P. Russell, *Annual Review of Materials Science*, **21**, 249 (1991).

[28] Information about the depth-dependence of the magnetic moment can be achieved at a synchrotron using XRR with circularly polarized light. However, the rotating anode Cu K α XRR we discuss is insensitive to sample magnetization.

[29] “Chemical” SLD is also referred to as “nuclear” SLD.

[30] G. M. Schott, W. Fashinger, and L. W. Molenkamp, *Appl. Phys. Lett.* **79**, 1807 (2001).

[31] I. Kuryliszyn-Kudelska, J. Z. Domagała, T. Wojtowicz, X. Liu, E. Łusakowska, W. Dobrowolski, and J. K. Furdyna, *J. Appl. Phys.* **95**, 603 (2004).

[32] *Neutron Data Booklet*, edited by Albert-José Dianoux, and Gerry Lander, (OCP Science, 2003).

[33] Only the real parts of the neutron and x-ray SLDs are plotted. For this system, the imaginary parts (absorption) are negligibly small for our purposes.

[34] W.H. Press et al., *Numerical Recipes, the art of scientific computing*, (Cambridge University Press, Cambridge 1986).

[35] http://www.ncnr.nist.gov/programs/reflect/data_reduction/software/index.html.

[36] J. F. Ankner and C. F. Majkrzak, *Neutron Optical Devices and Applications, SPIE Conference Proceedings*, Vol. 1738, edited by C. F. Majkrzak, and J. W. Wood (SPIE, Bellingham, WA, 1992), pp. 260-269.

[37] L.G. Parratt, Phys. Rev. **95**, 359 (1954).

[38] Using Hall Effect to measure carrier densities is not rigorously valid due to the contribution of the anomalous Hall Effect. However, this method is suitable to roughly compare p for our samples.

[39] X. Liu, Y. Sasaki, and J. K. Furdyna, Phys. Rev. B **67**, 205204 (2003).

[40] M. Sawicki, F. Matsukura, A. Idziaszek, T. Dietl, G. M. Schott, C. Ruester, C. Gould, G. Karczewski, G. Schmidt, and L. W. Molenkamp, Phys. Rev. B **70**, 245325(R) (2004).

[41] For all the neutron fits discussed in this paper it was the reflectivity that was fit – not the spin asymmetry.

[42] The χ^2 value discussed here is calculated from comparison of the spin-asymmetry data to the calculated spin asymmetry obtained from fits to the reflectivity. χ^2 for the reflectivity is also

significantly lower for the gradient model than for the flat model.

[43] Differences in substrate (or for the case of XRR, $\text{Ga}_{1-x}\text{Mn}_x\text{As}$) SLD between the two films are due to small differences in reflectometer alignment, and should be ignored. These alignment differences do not significantly affect the magnetic SLD, or the distribution of chemical SLD.

[44] *Center for X-Ray Optics and Advanced Light Source X-Ray Data Booklet*, Albert C. Thompson and Douglas Vaughan editors, (2nd edition, Lawrence Berkeley National Laboratory 2001).

[45] The presence of small amounts of indium should have no effect on the magnetic properties of $\text{Ga}_{1-x}\text{Mn}_x\text{As}$. We have grown and annealed many $\text{Ga}_{1-x}\text{Mn}_x\text{As}$ samples both with and without indium in the chamber, and have found it to have no effect on the resulting samples.

[46] In reference 18 we suggested that MnN might be present at an annealed film's surface. While that is consistent with the neutron data, a surface layer of *only* MnN is inconsistent with the x-ray data.

[47] For reasons of experimental convenience, this sample was not measured with H along the easy axis. However SQUID and PNR measurements of similar samples have shown that under the specified field and temperature conditions, the sample is magnetically saturated regardless of orientation.

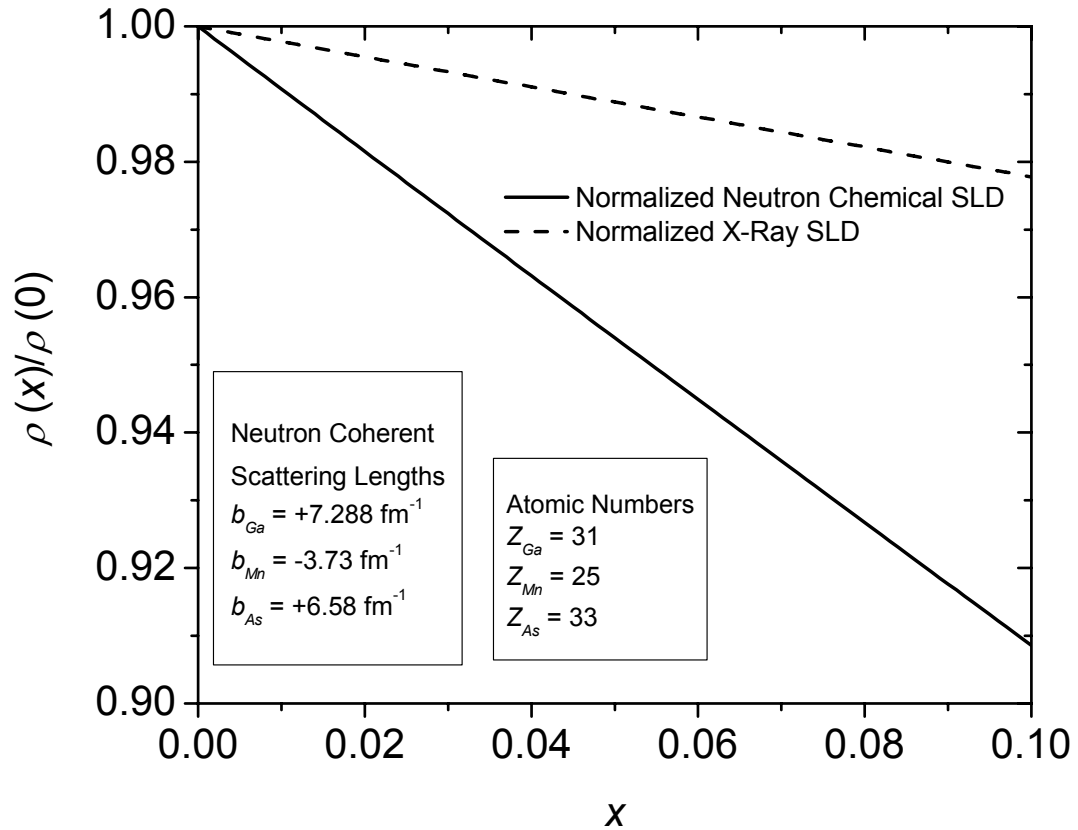


Figure 1: $\text{Ga}_{1-x}\text{Mn}_x\text{As}$ scattering length density (SLD) divided by GaAs SLD as a function of Mn doping x . The chemical component of the neutron SLD is much more sensitive to Mn doping than is the x-ray SLD, making neutrons far more sensitive to the $\text{Ga}_{1-x}\text{Mn}_x\text{As} / \text{GaAs}$ interface.

Set	As-Grown p (290 K) (10^{19}cm^{-3})	Annealed p (290 K) (10^{19}cm^{-3})	As-Grown \tilde{n}_{max} ($\Omega\cdot\text{cm}$)	Annealed \tilde{n}_{max} ($\Omega\cdot\text{cm}$)	As-Grown T_C (K)	Annealed T_C (K)
A	5.97	12.1	0.035	0.005	60	125
B	5.08	11.1	0.036	0.006	60	125
C	9.78	21.2	0.009	0.003	70	140

Table 1: Summary of the hole concentrations, resistivities and Curie temperatures of the three as-grown/annealed pairs discussed in this paper. Note that Set C is significantly different from the other two sets.

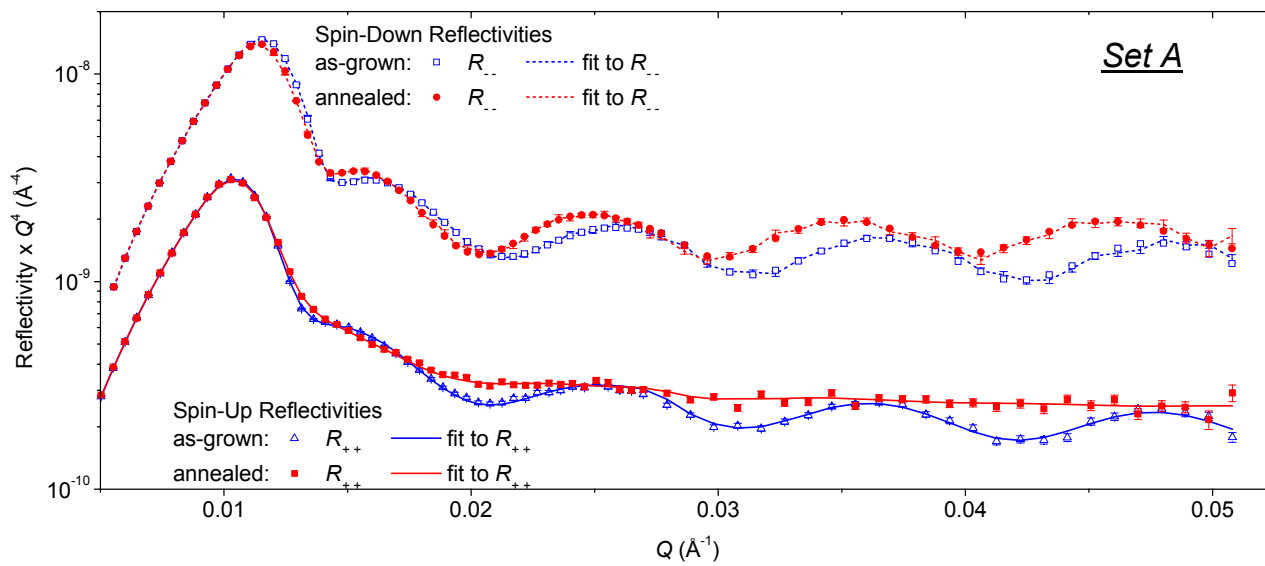


Figure 2 (Color online): Spin-down (top) and spin-up (bottom) reflectivities for the as-grown and annealed Set A films. The spin-down data has been shifted by an order of magnitude to allow for comparison.

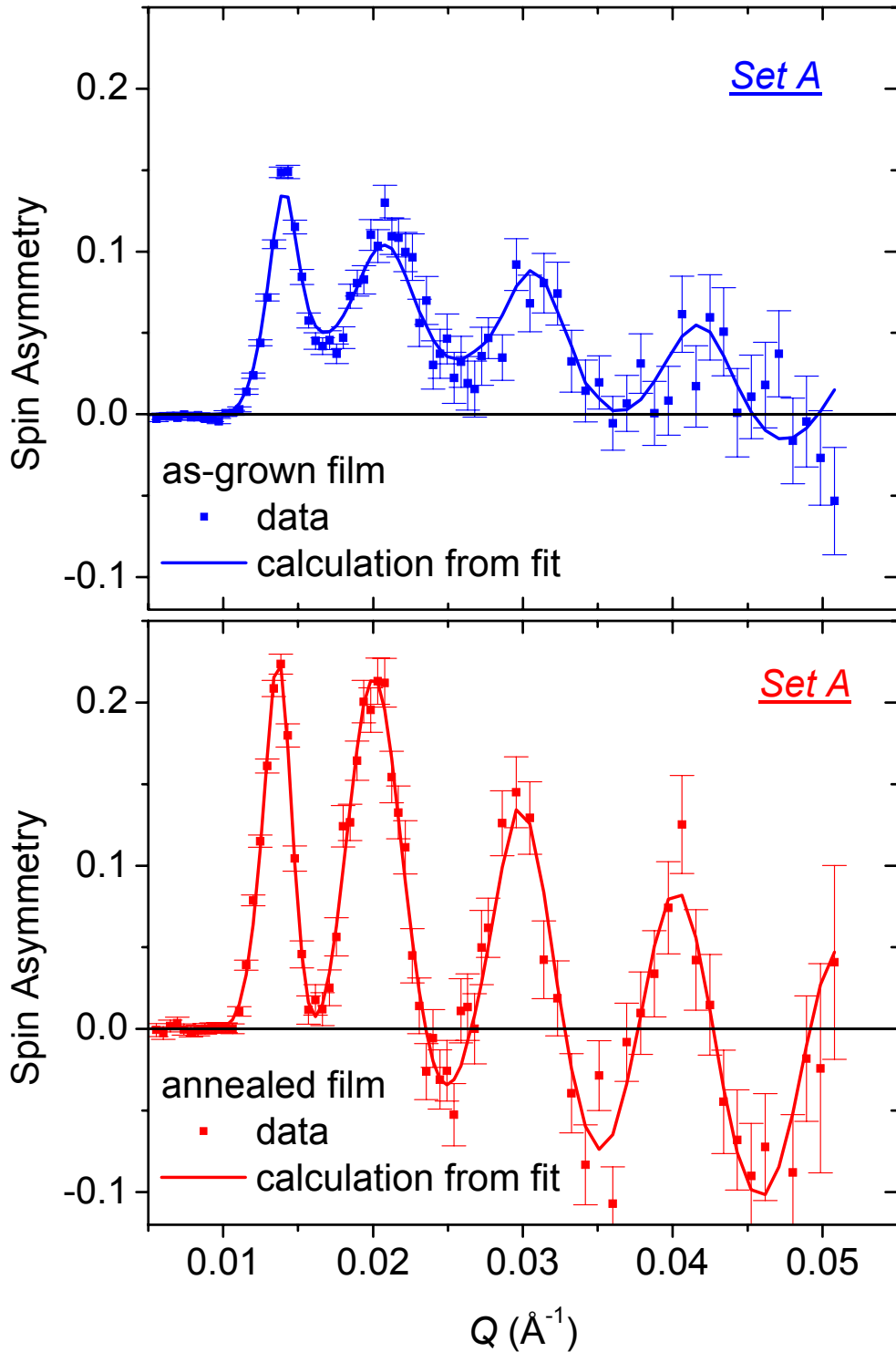


Figure 3 (Color online): Spin asymmetry for the Set A as-grown (top) and annealed (bottom) films.

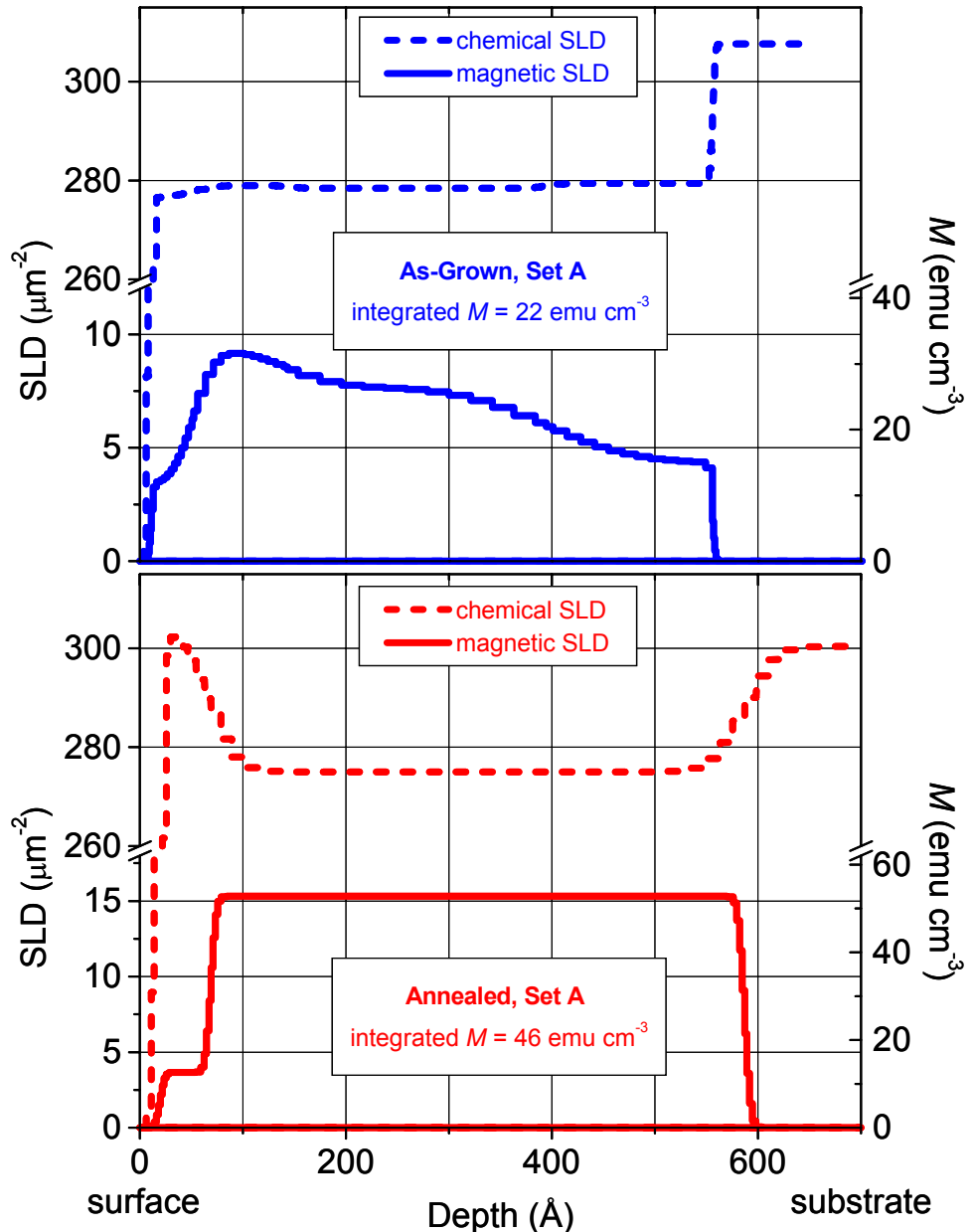


Figure 4 (Color online): Scattering length density models used to fit the PNR data in Fig. 2. The annealed film (bottom) has a larger integrated magnetization, a more homogeneous magnetization profile, and a chemically altered surface layer.

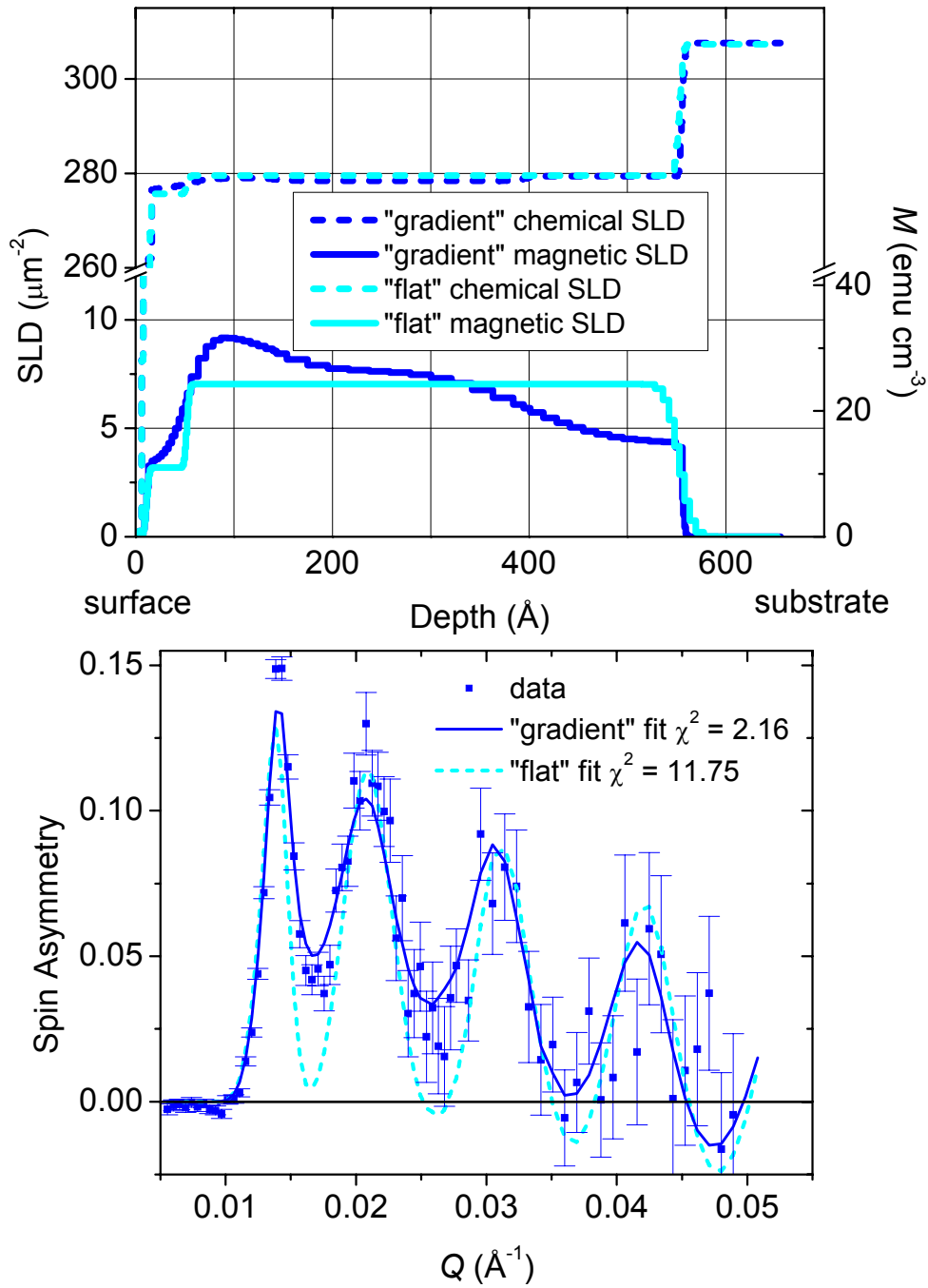


Figure 5 (Color online): Comparison of the “gradient” model and fit for the as-grown film (from Fig. 3-4) to an alternate “flat” model and fit. The flat model is not adequate to describe the data.

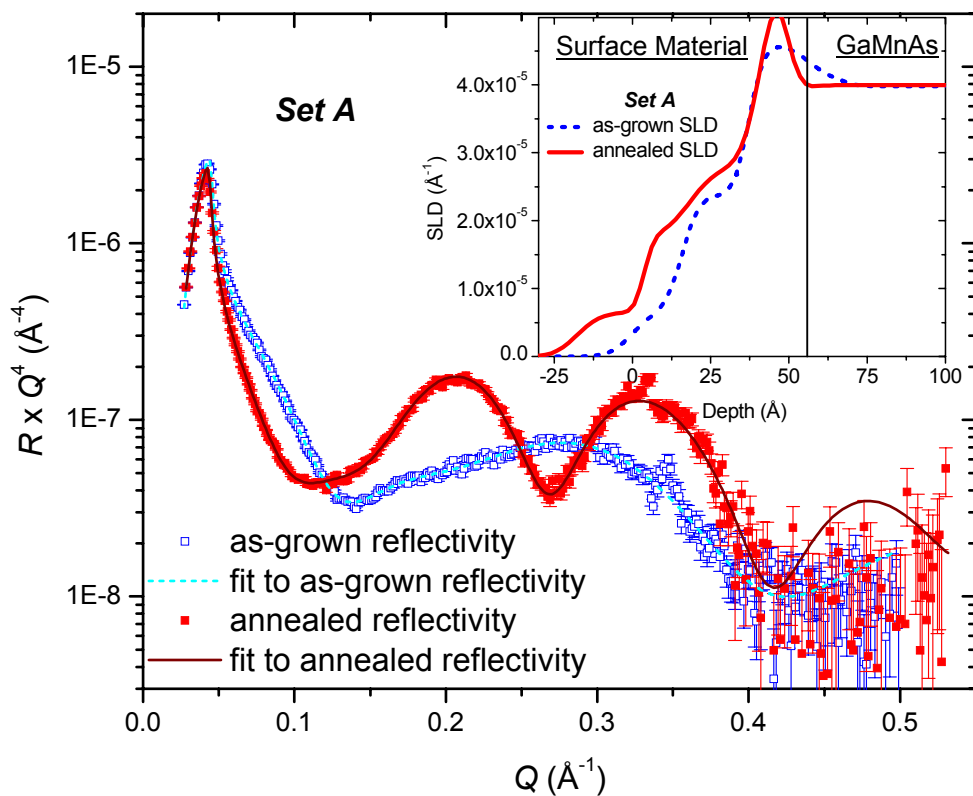


Figure 6 (Color online): XRR data, fits, and SLD models for the as-grown and annealed set A films.

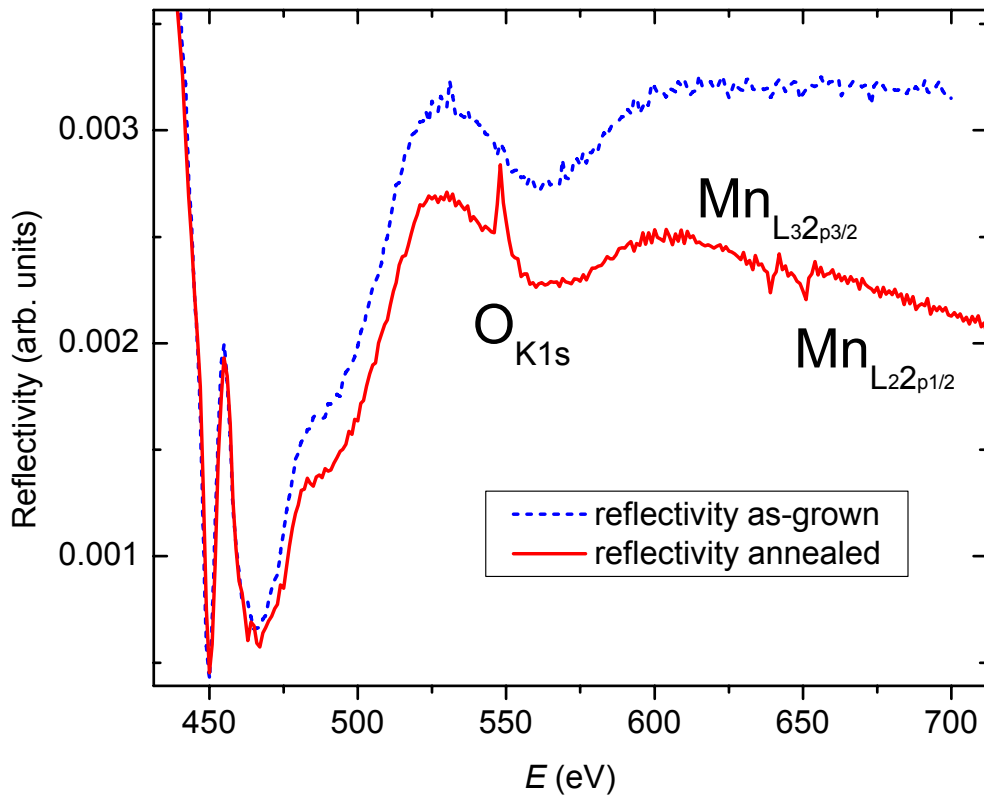


Figure 7 (Color online): Resonant XRR data for the as-grown and annealed set A films. The annealed film features pronounced O and Mn peaks while the as-grown does not.

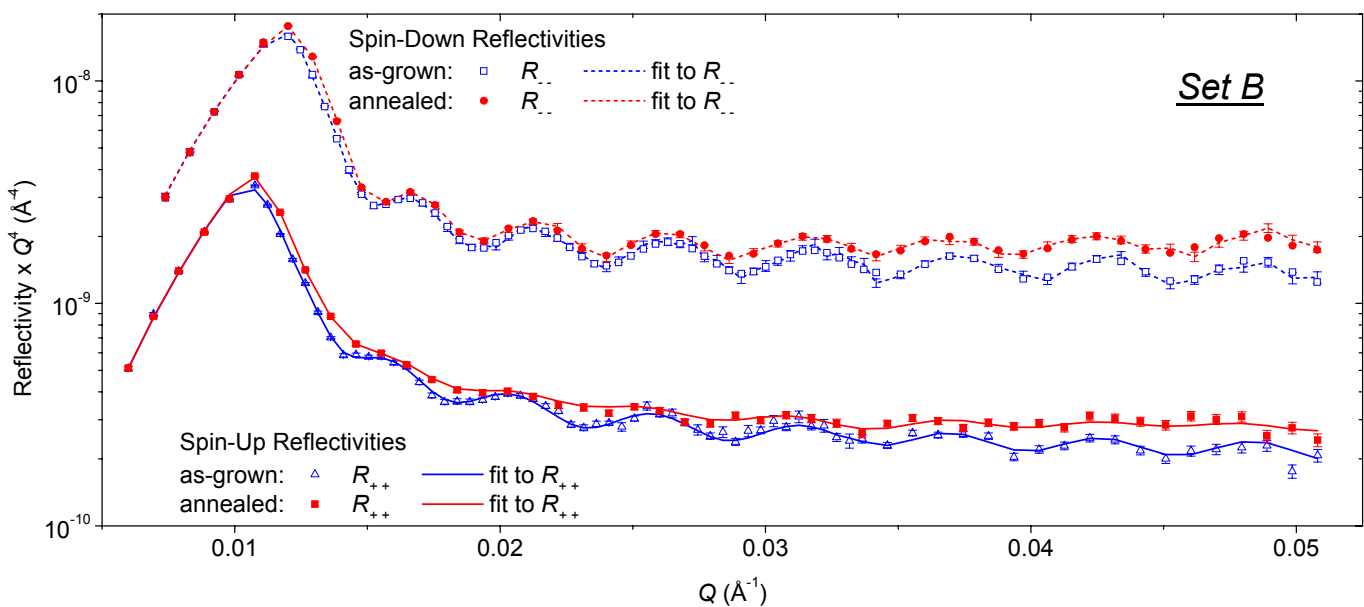


Figure 8 (Color online): Spin-down (top) and spin-up (bottom) reflectivities for the as-grown and annealed Set B films. The spin-down data has been shifted by an order of magnitude to allow for comparison.

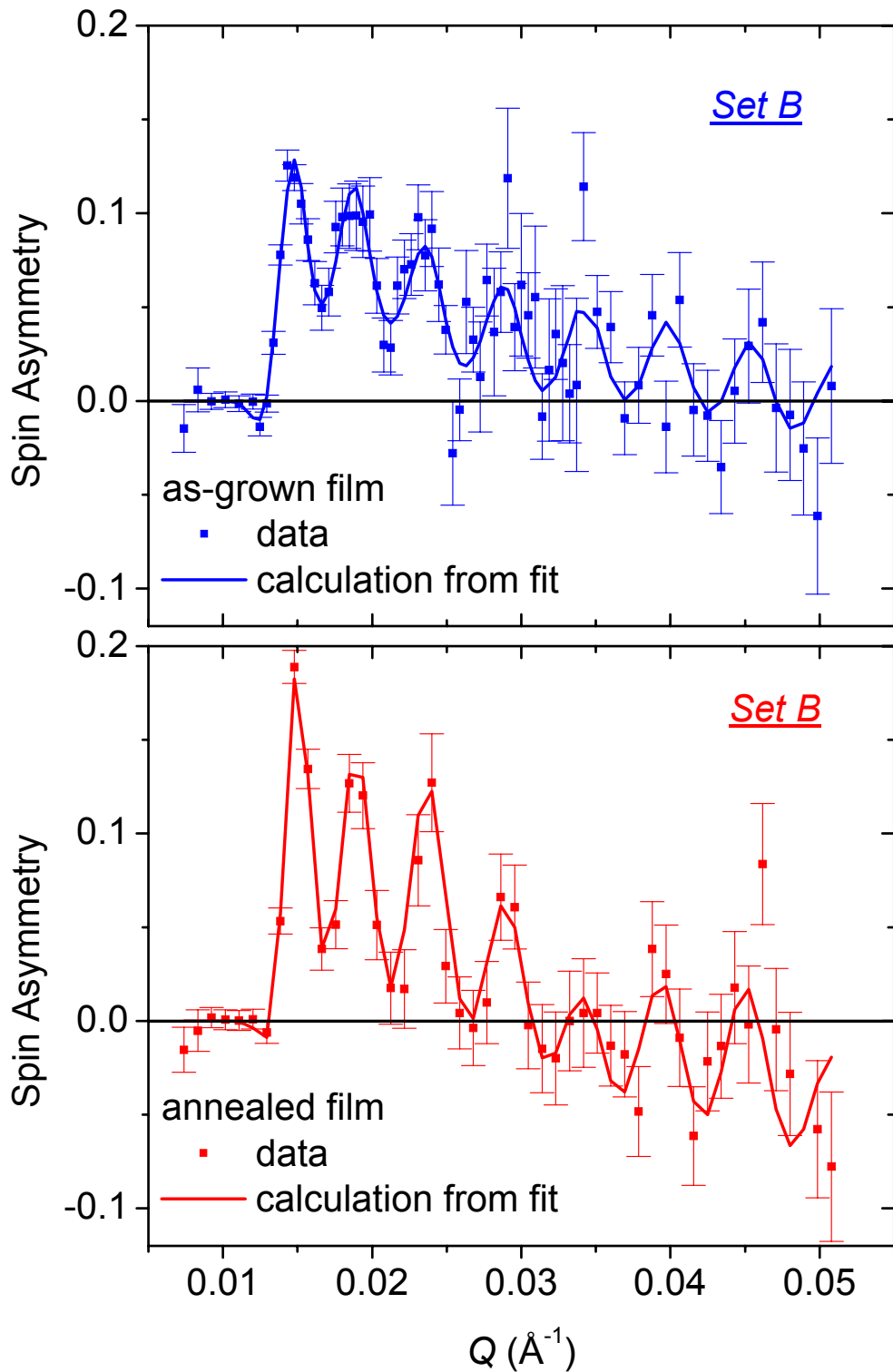


Figure 9 (Color online): Spin asymmetry for the Set B as-grown (top) and annealed (bottom) films. Reproduced from Ref.18.

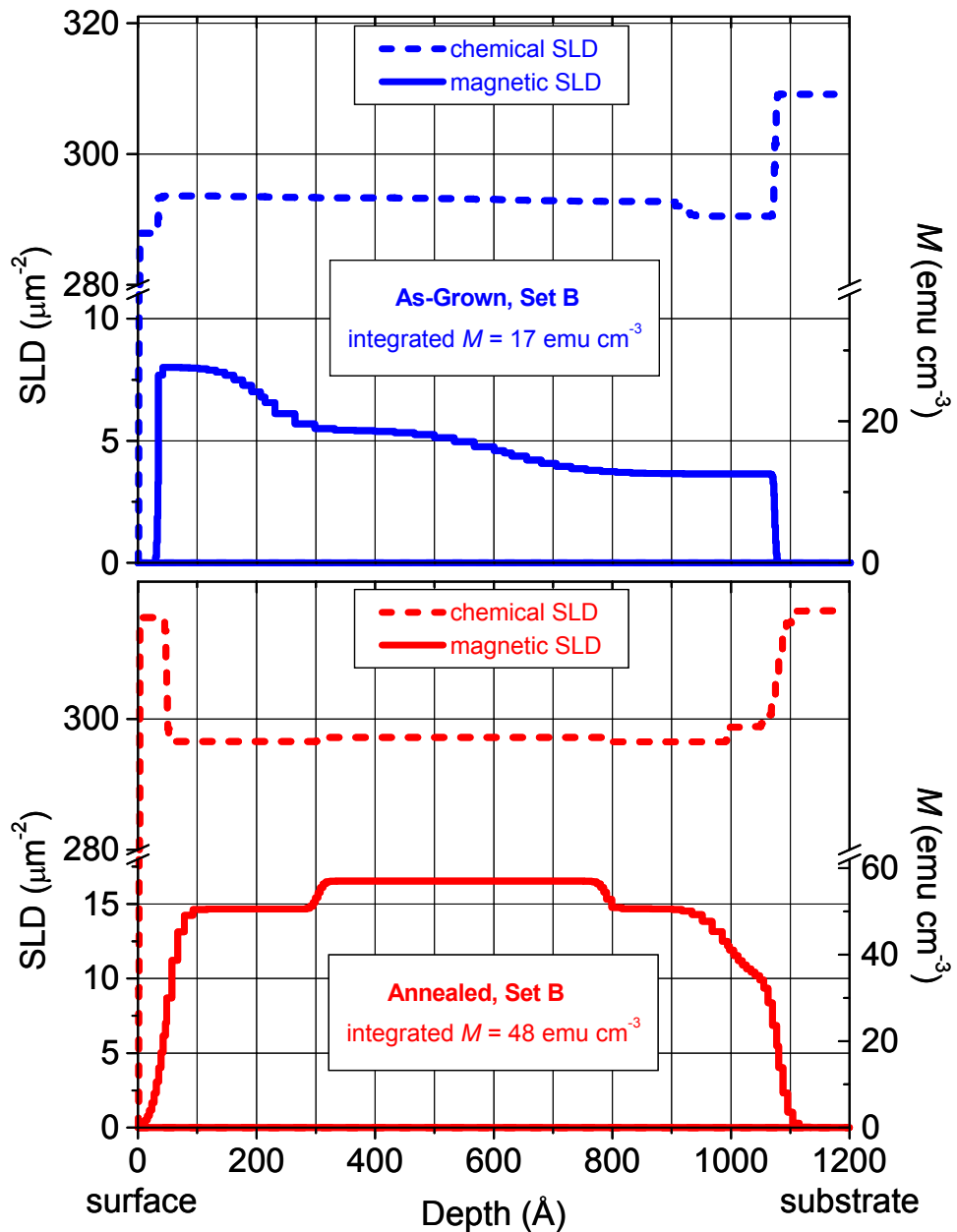


Figure 10 (Color online): Scattering length density models used to fit the PNR data in Figure 8. Reproduced from Ref. 18.

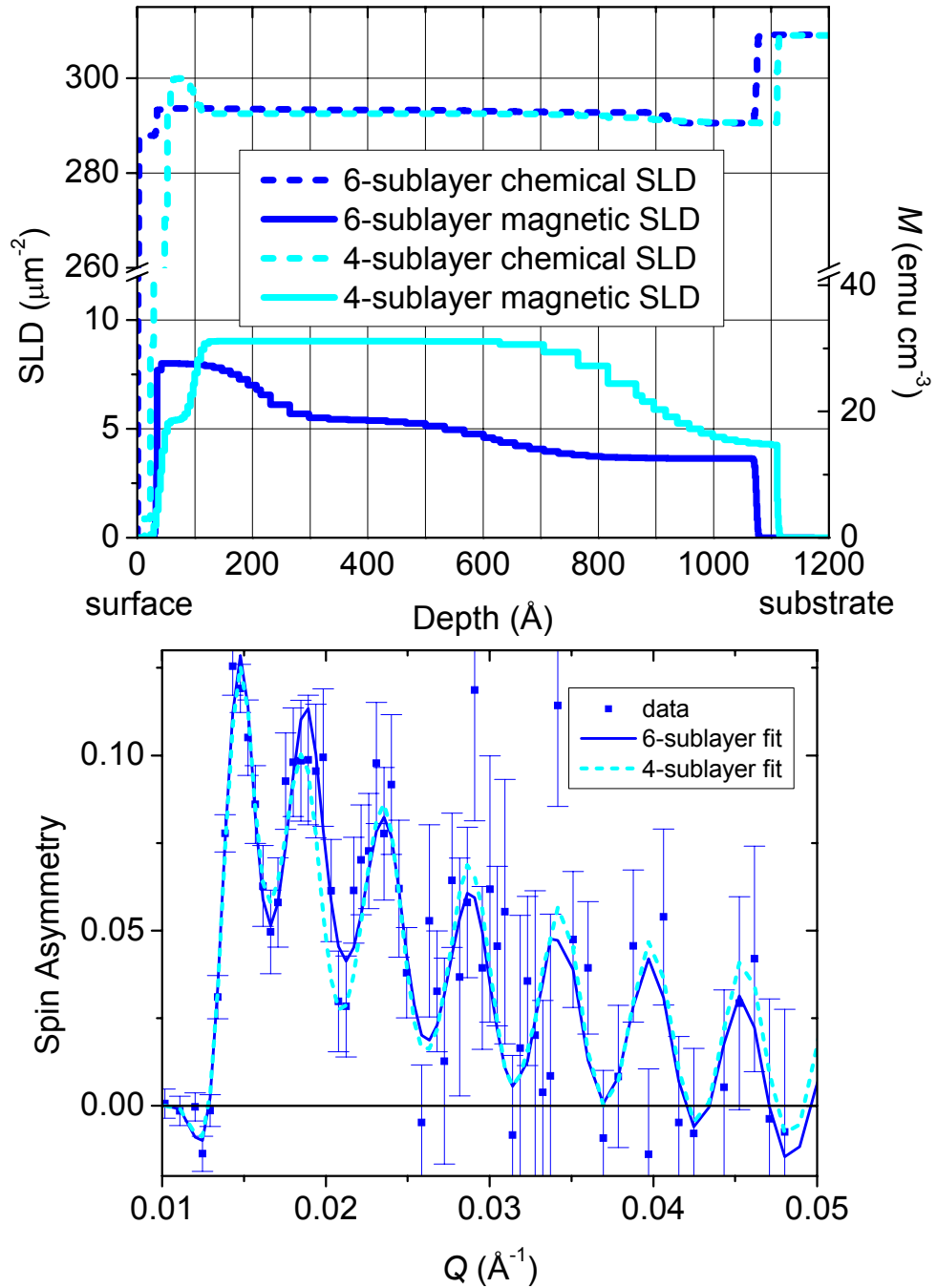


Figure 11 (Color online): Comparison of the 6-sublayer model and fit for the as-grown film (from Fig. 9-10) to an alternate 4-sublayer model and fit. The 4-layer model is only slightly worse at fitting the data - suggesting it is also a reasonable model.

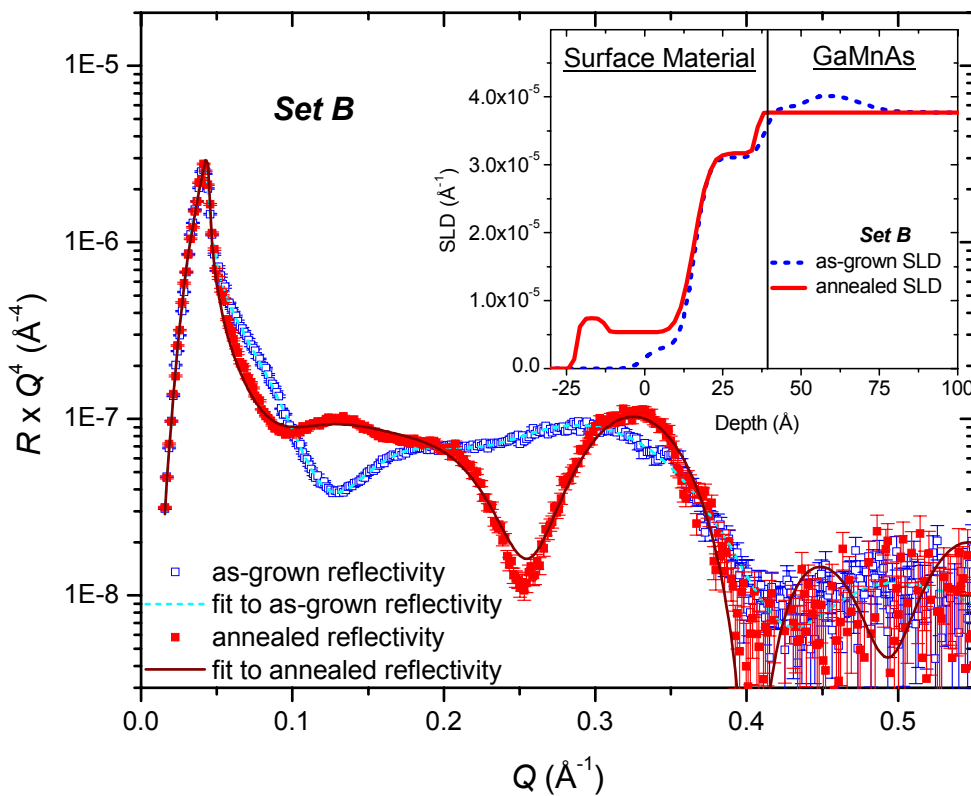


Figure 12 (Color online): XRR data, fits, and SLD models for the as-grown and annealed Set B films.

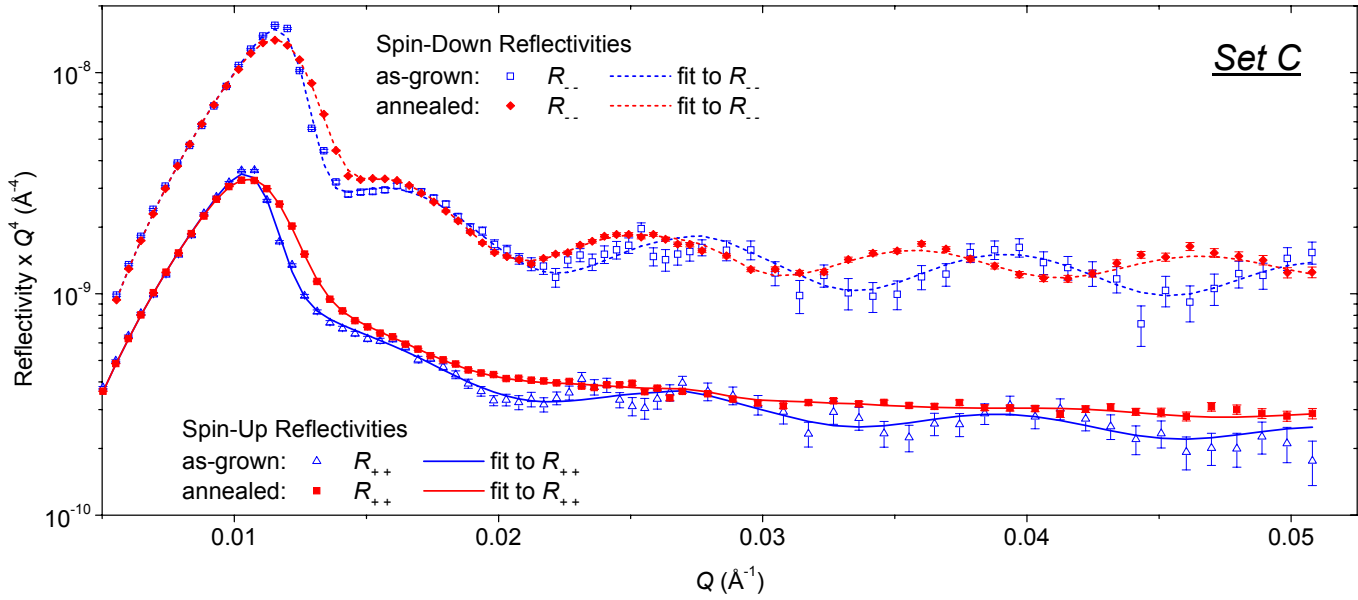


Figure 13 (Color online): Comparison of the as-grown and annealed Set C 50 nm films for each of the fitted NSF reflectivities. The spin-down data has been shifted by an order of magnitude to allow for comparison.

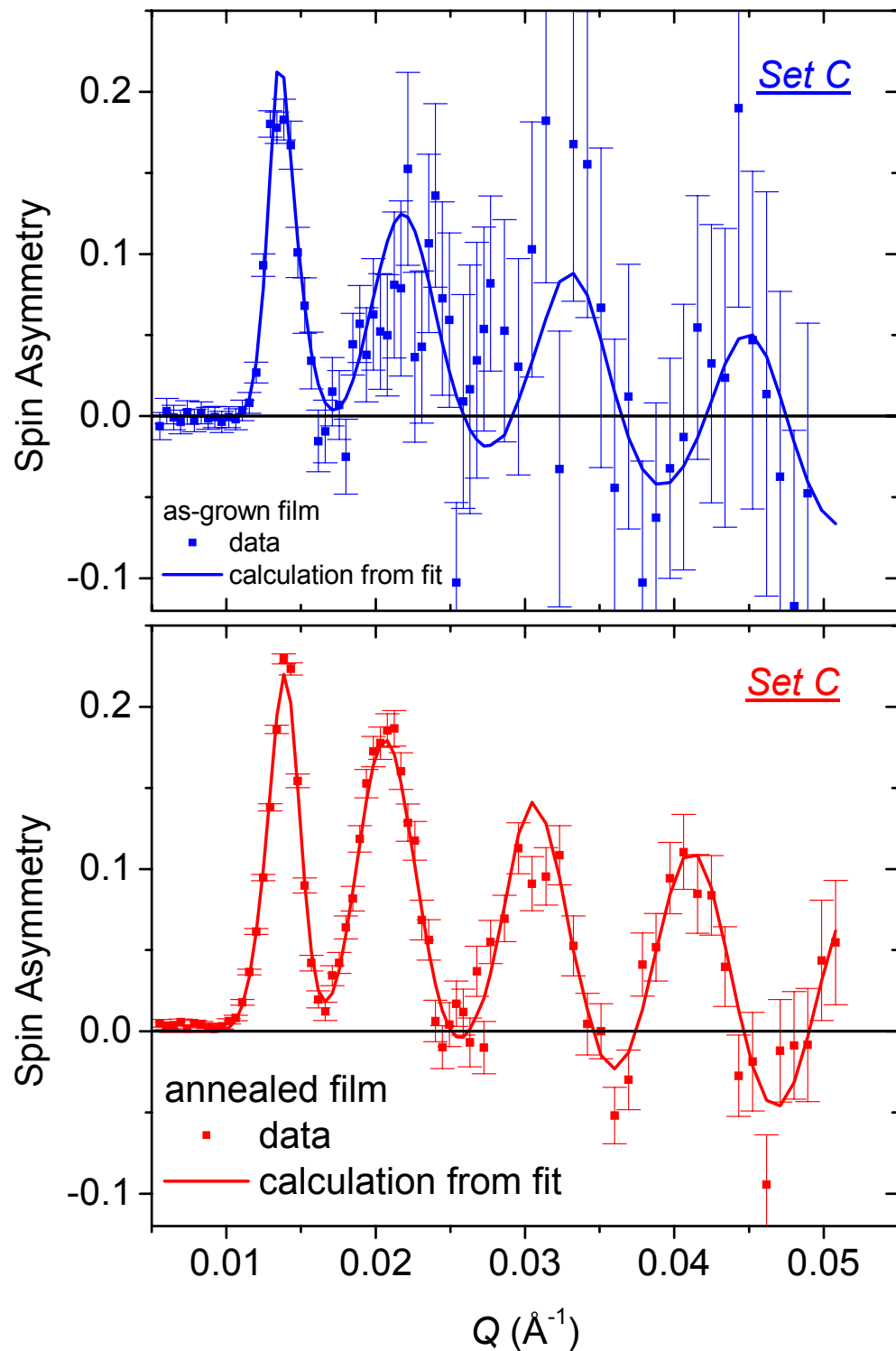


Figure 14 (Color online): Spin asymmetry for the Set C as-grown (top) and annealed (bottom) films.

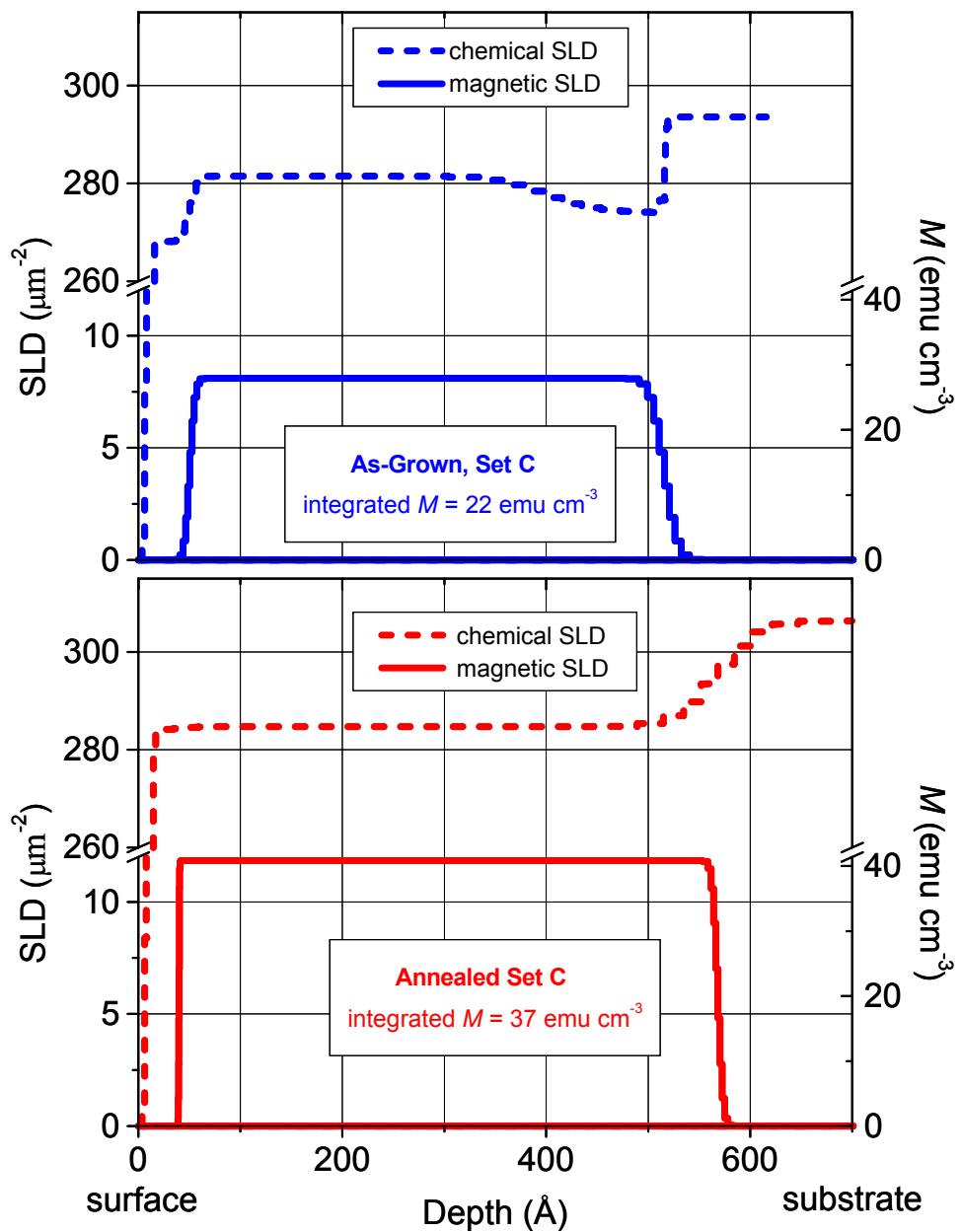


Figure 15 (Color online): Scattering length density models used to fit the Set C PNR data. Aside from a difference in integrated magnetization, the two models are quite similar.

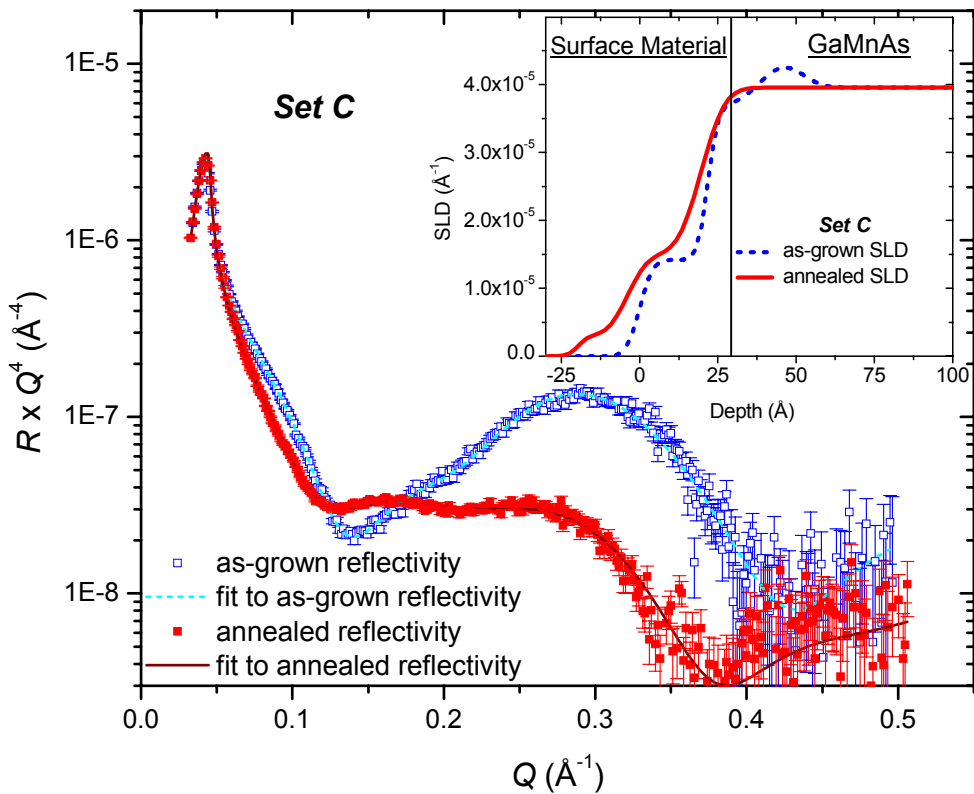


Figure 16 (Color online): XRR data, fits, and SLD models for the as-grown and annealed Set C films.

Figure Captions

1. Figure 1: $\text{Ga}_{1-x}\text{Mn}_x\text{As}$ scattering length density (SLD) divided by GaAs SLD as a function of Mn doping x . The chemical component of the neutron SLD is much more sensitive to Mn doping than is the x-ray SLD, making neutrons far more sensitive to the $\text{Ga}_{1-x}\text{Mn}_x\text{As} / \text{GaAs}$ interface.
2. Figure 2 (Color online): Spin-down (top) and spin-up (bottom) reflectivities for the as-grown and annealed Set A films. The spin-down data has been shifted by an order of magnitude to allow for comparison.
3. Figure 3 (Color online): Spin asymmetry for the Set A as-grown (top) and annealed (bottom) films.
4. Figure 4 (Color online): Scattering length density models used to fit the PNR data in Fig. 2. The annealed film (bottom) has a larger integrated magnetization, a more homogeneous magnetization profile, and a chemically altered surface layer.
5. Figure 5 (Color online): Comparison of the “gradient” model and fit for the as-grown film (from Fig. 3-4) to an alternate “flat” model and fit. The flat model is not adequate to describe the data.
6. Figure 6 (Color online): XRR data, fits, and SLD models for the as-grown and annealed Set A films.
7. Figure 7 (Color online): Resonant XRR data for the as-grown and annealed Set A films. The annealed film features pronounced O and Mn peaks while the as-grown does not.
8. Figure 8 (Color online): Spin-down (top) and spin-up (bottom) reflectivities for the as-grown and annealed Set B films. The spin-down data has been shifted by an order of magnitude to allow for comparison.
9. Figure 9 (Color online): Spin asymmetry for the Set B as-grown (top) and annealed (bottom) films. Reproduced from Ref.18.
10. Figure 10 (Color online): Scattering length density models used to fit the PNR data in Figure 8. Reproduced from Ref. 18.
11. Figure 11 (Color online): Comparison of the 6-sublayer model and fit for the as-grown film (from Fig. 9-10) to an alternate 4-sublayer model and fit. The 4-layer model is only slightly worse at fitting the data - suggesting it is also a reasonable model.
12. Figure 12 (Color online): XRR data, fits, and SLD models for the as-grown and annealed Set B films.
13. Figure 13 (Color online): Comparison of the as-grown and annealed Set C 50 nm films for each of the fitted NSF reflectivities. The spin-down data has been shifted by an order of magnitude to allow for comparison.

14. Figure 14 (Color online): Spin asymmetry for the Set C as-grown (top) and annealed (bottom) films.
15. Figure 15 (Color online): Scattering length density models used to fit the Set C PNR data. Aside from a difference in integrated magnetization, the two models are quite similar.
16. Figure 16 (Color online): XRR data, fits, and SLD models for the as-grown and annealed Set C films.